Thermal decomposition of $CuProp_2$: in-situ analysis of film and powder pyrolysis

Silvia Rasi[1,2], Fabrizio Silveri[3], Susagna Ricart[2], Xavier Obradors[2], Teresa Puig[2], Pere Roura-Grabulosa[1] and Jordi Farjas[1]

[1] University of Girona, Campus Montilivi, Edif. PII, E17003 Girona, Catalonia, Spain
[2] Institut de Ciència de Materials de Barcelona, ICMAB – CSIC, Campus UA Barcelona, E-08193 Bellaterra, Catalonia, Spain
[3] Cardiff University, Department of Chemistry, Park Place, Cardiff, CF24 3AT, United Kingdom

*Corresponding author: Silvia Rasi, silvia.rasi@udg.edu; srasi@icmab.es

Abstract

The thermal decomposition of $CuProp_2$ in the form of film and powder was studied in different atmospheres by means of thermal analysis techniques (TG-MS, TG-IR, EGA), chemical-structural methods (FTIR, XRD, EA) and computational thermochemistry (VASP/PBE). The decomposition mechanism in terms of volatiles evolved was disclosed with the aid of ab-initio modeling; it was found to be dependent on the gas diffusion in and out of the sample and accelerated by a humid atmosphere. In films, the copper redox behavior showed sensitivity to the residual atmosphere. Finally, the role of the metal center is discussed in the frame of a general decomposition mechanism for metal propionates.

Keywords: Copper propionate; pyrolysis; thermogravimetric analysis; evolved gas analysis; metal carboxylates; CSD methods

1. Introduction

The study of the thermal decomposition of metal carboxylates has been growing in the past years as a consequence of their role in the synthesis of functional oxide thin films. Among the latter, $YBa_2Cu_3O_{7-\partial}$ (YBCO) belongs to the II generation of High Temperature Superconductors (HTS) [1]; it is processed for tapes applications in fields such as energy transport and electrical power devices [2]. However, nowadays, its use for these applications is limited by its production costs, which rely on physical methods like molecular beam epitaxy (MBE), pulsed laser deposition (PLD) and sputtering. Therefore, it has become of the utmost importance to develop a cost-effective synthetic route for YBCO films to be, then, transferred to tapes synthesis. In this regard, chemical solution deposition of metal organic precursors (CSD-MOD) [3,4] is known to be a good candidate to fulfil this challenge. CSD is based on two main steps, pyrolysis of the organic material after deposition on a substrate, and growth of the oxide from the inorganic intermediates. Since removal of all organic material is important, usually short chain metal salts are the chosen starting material for the precursor solution. As both steps need to be optimized for the final film's properties and performance, an increasing number of studies can be found concerning growth analysis [5] and pyrolysis of metal salts like propionates and acetates of yttrium [6–9], copper [3,10–15] and barium [16,17].

However, although CSD-MOD methods are based on thin film processing, so far $Cu(CH_3CH_2CO_2)_2$ ($CuProp_2$) decomposition has only been studied for samples in the form of

powder. Additionally, while several references can be found for the thermal analysis of $CuProp_2$ [15] or other carboxylates [18,19], an extensive analysis in terms of atmospheres and decomposition volatiles has not yet been done.

Volatile species evolved during decomposition can be detected by means of thermogravimetry (TG) coupled with Evolved Gas Analysis (EGA), which mainly works by infrared (EGA-FTIR or TG-FTIR) or by mass spectrometry (EGA-MS or TG-MS) detection. In fact, by EGA-FTIR and EGA-MS, it was shown that the decomposition of propionates in inert atmospheres involves formation of radicals $C_2H_5\cdot$ and $C_2H_5CO\cdot$ (along with CO_2) and their recombination to form a symmetrical ketone [20–22]. For longer chain salts such as Ca(II)decanoate, techniques like pyrolysis coupled to gas chromatography (GC) revealed a more complicated scenario where normal alkanes were found along with several symmetrical ketones [23]. For odd chain length of Cu(II)carboxylates like Cu(II)propionate, only MS has been used for the in-situ EGA analysis and 2-pentanone (asymmetrical ketone) was reported to be the main decomposition product [11]. Formation of this asymmetrical ketone implies cleavage of a C–C(C=O) bond, instead of the expected C–C(=O) and C(=O)–O bonds. Conversely, no ketones at all were observed for even chain carboxylates of copper(II) [24], mercury(II) [25] and silver(I) [26]. In fact, references [24,25] report on the decomposition of even chain length of Hg(II) and Cu(II) carboxylates as involving formation of ethylene and propionic acid along with CO_2. Clearly, there is no univocal decomposition pathway for metal carboxylates, on the contrary it depends on the surrounding atmosphere, the length of the carboxylate chain and the type of metal ion [27].

The aim of this paper is to disclose the thermal decomposition mechanism of $CuProp_2$. For this purpose, thermogravimetry combined with in-situ EGA analysis is used and different atmospheres are considered. Also, samples in the form of film and powder are analyzed and characterized by Fourier-transform infrared spectroscopy (FTIR), elemental analysis (EA) and X-ray diffraction (XRD). In situ TG-FTIR, TG-MS and EGA-MS allow an almost univocal identification of the volatiles, while the comparison of experimental enthalpies with theoretical data will show which of the proposed decomposition reactions takes place in a given atmosphere.

We will show that $CuProp_2$ decomposes releasing the corresponding acid as major product and we propose a mechanism that is compatible with the observed phases and detected volatiles. We also show that the kinetics depends on sample preparation and atmosphere; in particular that decomposition is significantly enhanced in the presence of water vapor and in films.

2. Materials and methods

The initial solution was obtained by dissolving copper(II) acetate ($Cu(CH_3CO_2)_2$ Sigma Aldrich, 0.75M), dried in vacuum at 60°C, in a 1:1 mixture of methanol (VWR, ≥99.8%) and propionic acid (Merck, ≥99%). Deposition of that solution over 10x10 mm^2 or 5x5 mm^2 $LaAlO_3$ (LAO) substrates was followed by drying at 95°C on a hot plate for a few minutes. The initial product after deposition is expected to be $Cu(C_2H_5CO_2)_2$ ($CuProp_2$), since in an excess of propionic acid, acetate groups are replaced by propionates [28]. The corresponding powder was recovered upon solvent evaporation in air at 90°C. For comparison, $CuProp_2$ in the form of powder and film was studied by FTIR, XRD and elemental analysis; no differences were observed (See Fig. S2). A single crystal was also obtained after a few-month storage of the solution at room temperature; it was recovered and dried at 30°C and low vacuum (635 mmHg) prior to analysis.

The "nominal film thickness" h is determined from the mass (m) of the sample, the substrate area (A), and the particle density (ρ) of the final product (CuO) as $h = \frac{m}{\rho A}$. Calculated thicknesses for the films used in this work ranged from 1.9-2.1 µm.

Since the density of the films is lower than the particle density, the nominal thickness is a

lower-bound estimation of the real thickness of the pyrolyzed film.

TG analysis of $CuProp_2$ as film and in the form of powder was carried out in a Mettler Toledo thermo-balance, model TGA/DSC1. Samples were heated at a constant rate of 5°C/min under a dynamic atmosphere (flow rate of 55ml/min of carrier gas and 15ml/min of the protective gas). Water-saturated gas was obtained by bubbling the carrier gas in a water flask at standard temperature and pressure (25°C, 1 atm). Under these conditions the saturated vapor partial pressure is 3.1% [29]. LAO substrates were used for films deposition, whereas uncovered 70-µl-Al_2O_3 pans were used for the powder sample. In-situ TG-FTIR or TG-MS were performed to monitor the evolution of the volatiles during sample decomposition. In the first case, the TG was coupled to the gas cell (Bruker ALPHA model) through a 40-cm-long steel tube kept at 200°C. For TG-MS a steel capillary heated up to 200°C was connected from the TG gas outlet to the MS chamber and the fragments were detected by means of a quadrupole mass analyzer (MKS model Microvision Plus).

In the case of samples decomposed directly in vacuum (EGA-MS), volatiles are detected without the need of a steel capillary: the film or crucible with the powder are placed on a platinum plate inside a quartz tube that is pumped to a total pressure of 10^{-6} bar by means of a rotative pump in series with a turbomolecular pump. The sample temperature is measured with a thermocouple soldered to the platinum plate and controlled with an external tubular furnace placed around the quartz tube. Interpretation of the MS spectra of the volatiles was done according to NIST reference spectra, but it should take into account that the fragmentation pattern of the analyte can show temperature dependence in favor of lower molecular weight fragments [30,31].

X-ray diffraction curves (XRD) of powders and films (the latter were peeled off to be measured) were collected using an X-ray beam wavelength of 1.5406 Å (Cu-Kα) from two different diffractometers: a Siemens diffractometer (model D-5000) from Bruker, operating at a 35-mA current and at a voltage of 45 kV; and a D8 ADVANCE diffractometer from Bruker AXS, with an X-ray beam of Cu-Kα, operating at a 40-kV voltage and with a 40-mA current. Single-crystal X-ray diffraction was performed with a three-circle diffractometer (Bruker D8 QUEST ECO) system equipped with a Ceramic x-ray tube (Mo Kα, λ = 0.71076 Å) and a doubly curved silicon crystal monochromator. The measurements were made at 50 kV and 20 mA and x-rays collected by a PHOTON II (CPAD, Charge-Integrating Pixel Array Detector) detector.

Infrared analysis of solid samples was performed using a Fourier Transform Infrared Spectrometer (FTIR, Bruker model ALPHA) equipped with an attenuated total reflection (ATR) unit (model Platinum), while a Perkin Elmer 2400 series elemental analyzer was used for Elemental Analysis (EA).

Six TG-FTIR/MS experiments were conducted at atmospheric pressure varying the flowing gas: $CuProp_2$ as film was decomposed in humid O_2 (experiment **A**), humid N_2 (**B**) dry O_2 (**C**) and dry N_2 (**D**); the powder sample (labeled with **'**) was decomposed in dry O_2 (**C'**) and dry N_2 (**D'**). To avoid N_2 interference with CO detection (both with m/z=28), **D'** was performed in argon for TG-MS. EGA-MS experiments were run on the film (**E**) and powder (**E'**, **E''**) samples, at 5°C/min, 10 and 25°C/min, respectively.

Ab-initio theoretical calculations were performed within the framework of Density Functional Theory (DFT) as implemented in the VASP (Vienna Ab-initio Software Package) code [32,33]. All models are periodically replicated through space in all directions, in order to obtain a more accurate description of the solid phases investigated experimentally, as no boundary effects are to be taken into consideration. The theoretical investigation of $CuProp_2$ and CuO was designed to accurately model their electronic structure as a bulk solid. Database structure files were converted into periodic models. The experimental unit cell was relaxed towards the computational

minimum energy structure, identified using a built-in DIIS minimization algorithm with a convergence force threshold of 10^{-2} eV/Å. The electronic structure was evaluated differently for gas phase and solid phase systems. For the former, a single K-point was considered sufficient to evaluate the electronic structure, due to the unit cell size having been optimized to minimize the interaction between different replicas of the molecule. For the latter, a K-point grid was obtained using the Monkhorst-pack method and its size was optimized until further increases did not correspond to any change in total energy. More details can be found in Supp. info.

3. Results

3.1 Characterization of the initial product

In excess propionic acid, acetate groups are replaced by propionates. In fact, the elemental analysis results of the dry salt are in good agreement with the expected values for $CuProp_2$ (Table 1), and with the EA results of $CuProp_2$ obtained from an acetate-free solution (by reacting $CuCO_3$ in excess propionic acid, see Supp. Info, Table S1). Additionally, the FTIR spectrum of the film displayed in Fig. 1 coincides with the reported assignments in [34]. The single-crystal analysis (see Supp. Info, Fig S1-a) performed on our single-crystal corresponds to the anhydrous $CuProp_2$ database structure (CCDC 1133510) [35], which consists of Cu dimers connected by bridging carboxylate ligands. Since the XRD powder-diffraction curve of the ground crystal (Fig. S1-c) coincides with that of our films (Fig. 1, inset), this structure (CCDC 1133510) was used later on for ab-initio calculations. In fact, our films' magnetic behavior (see Supp. Info) is as expected for binuclear copper complexes where an antiferromagnetic super-exchange interaction exists between the Cu(II) atoms [36–38] due to bridging ligands, and which is responsible for the lower magnetic moment, μ_{eff}, in $CuProp_2$ crystalline powders with respect to Cu(II) compounds in aqueous solutions (exp. range of 1.9-2.2 μ_B) [39,40]. In fact, by comparing the distance between the asymmetric and symmetric stretching band of the carboxylate bond [41,42] [$\Delta v = \nu_{as}(COO^-) - \nu_s(COO^-)$] of our $CuProp_2$ with those of other carboxylates from literature, our Δv=165 cm^{-1} value suggests a bridging ligand coordination [43,44].

Coordination water is expected to change the structure, but the OH stretching band of water does not increase significantly over time, indicating that $CuProp_2$ is not very hygroscopic.

3.2 Thermal decomposition of $CuProp_2$ at atmospheric pressure in film

During sample preparation, no water uptake is observed after drying the film at 95°C Therefore, no dehydration is observed in the thermogravimetric analysis and DSC (Fig. 2a and b, respectively); the first mass loss step corresponds to the ligand decomposition. The main volatiles evolved during this step are identified in the TG-FTIR spectra in Fig. 3 and their detailed evolution as a function of atmosphere and temperature is shown in Fig. 4.

The general decomposition mechanism for films involves two stages (labeled as I and II in Fig. 2a) to yield CuO at 500ºC (Fig. 5a exp. **A**,**C**,**D**). Most of the mass loss (≈92%) takes place during the first stage and involves formation of propionic acid (Fig. 3). From Fig. 2a, the first stage is not influenced by the presence of O_2 but it is accelerated by the presence of a humid atmosphere, and in fact step I in **A** (humid O_2) and **B** (humid N_2) ends at 190°C, whereas it ends 10°C above in **C** (dry O_2) and **D** (dry N_2). Therefore, H_2O vapor shifts the TG curve to low temperatures because it favors the hydrolysis of the salt through reaction scheme **α** (Table 2); this shift is enhanced for thinner films (Supp. Info, Fig. S9), indicating water vapor diffusion to be the reaction-rate limiting mechanism. So, for instance, in humid O_2, $CuProp_2$ XRD reflections disappear and CuO crystalizes between 185 and 210°C (Fig. 5b, **A**). Conversely, in dry N_2, CuO crystallization is delayed to 195°C-

215°C (Fig. 5b, **D**). For any atmosphere, a change in the $CuProp_2$ structure is observed during its decomposition as $\Delta\nu_{COO^-}$ decreases from 165 to 125 cm^{-1} (Fig. 6 and Supp. Info, Fig. S5). Similarly, the molar magnetic susceptibility at different decomposition stages (Supp. Info) shows that the antiferromagnetic interactions decrease with increasing paramagnetic Cu(II) contribution, probably due to the breaking of the copper(II) carboxylate dimers [45].

After the first stage, a plateau in the TG curve is observed at $m_f/m_i \approx 42\%$ (200-230°C), corresponding to an intermediate product with a change of decomposition mechanism. The films quenched at ~200-230°C are dark, and in all atmospheres, their FTIR absorptions (Fig. 6**A** and 6**D**) show the presence of residual carboxylate and copper oxide (bands below 500 cm^{-1}), with a high Cu/propionate ratio (combining EA and TG results: $Cu_{12}O_{14}C_3H_4$), and a lower carbon content (Table 1) than the theoretical value for copper carbonates (6-10%)[46]. This harder-to-decompose intermediate may suggest the formation of CuO clusters stabilized by the remaining propionates, similarly to the way nanoparticles have been reported to form from solvent-less routes [47], although usually synthesized through wet chemistry [48,49]. This intermediate later decomposes producing mostly acetaldehyde (from oxidation of C_2H_5 fragments of the ligand) and CO_2.

This second decomposition stage is accelerated by oxygen and it is not affected by humidity (see Fig. 2): in oxygen, decomposition occurs at 220°C (solid lines in Fig. 2, **A** and **C**), whereas without oxygen, **B** and **D**, it is delayed to 240 and 260°C, respectively (dashed lines in Fig. 2; this stage occurs at even higher temperatures in more inert atmosphere, Fig. S9). Apparently, stage II involves oxidation because the mass-loss step is accompanied by an exothermic DSC peak (Fig. 2b). This is in agreement with reaction scheme **β** (Table 2). Except for the experiment in dry N_2 (**D**), the sample mass is quite stable beyond 260°C. Furthermore, in all films at 500°C, XRD analysis reveals only the presence of CuO (Fig. 5a, **A**), and EA (Table 1) confirms that neither carbon nor hydrogen is left.

Only in the case of dry N_2, this second step coincides with Cu(II)O reduction to $Cu(I)_2O$ (Fig. 5b, **D**) upon CO_2 evolution (Fig. 4, **D**) at 260°C. The fact that Cu(I) is obtained out of the Cu(II)-Cu(I) thermodynamic equilibrium conditions suggests a redox reaction between the remaining carbon (4% in Table 1) and CuO. In fact, a sample heated in humid O_2 and quenched before the II stage begins, experiences CuO reduction (like in **D**) when heated in vacuum, releasing CO_2 and CO (shown in Supp. Info). However, by 350°C, given the high sensibility of films to residual oxygen, the Cu_2O film is oxidized again to CuO (Fig. 5a, **D**), and at 500°C no carbon and hydrogen are left (Table 1). Finally, note that the presence of water vapor (**B**, humid N_2) is enough to prevent this reduction.

To further confirm these decomposition reactions and exclude any possible influence of remaining acetate ligands, the decomposition of a powder obtained from an acetate-free precursor solution ($CuCO_3$ in excess propionic acid) was studied as a comparison, spread on a LAO substrate to approach the conditions of experiment **A**. The decomposition temperatures were very similar and the volatiles were the same as in exp. **A**, confirming that the reaction schemes proposed are the expected ones for the decomposition of $CuProp_2$ (see Fig. S3 in Supp. Info).

3.3 Thermal decomposition of $CuProp_2$ at atmospheric pressure in powder

For "bulk" $CuProp_2$ powder (m_i of tens of mg), the residual water vapor in nominally dry O_2 (**C'**) and N_2 (**D'**) atmospheres has no effect on decomposition and, consequently, powders decompose at much higher temperatures (≈ 250°C, Fig.2a) than films.

In dry N_2 (**D'**), decomposition is endothermic (Fig. 2b), which is consistent with the reduction of copper (like in process **γ** of Table 2). XRD and FTIR measurements (see Fig. 5b and Fig.

6 **D'**, respectively) on samples quenched at ~250-265°C, around the mass derivative discontinuity, indeed reveal the formation of Cu_2O; just after quenching from 265°C, a fraction of the sample is liquid, and green portions emerge as it quickly solidifies, resulting in an XRD peak at 2θ=6.5 (△ in Fig. 5b, **D'**, 260°C) and new C=O FTIR bands (△ in Fig. 6 **D'**) at 1740 cm^{-1}. In fact, the sample mass loss at this temperature (65% m_f/m_i) is in agreement with Cu(I)Prop formation, but the XRD peak at low angles might suggest its oxidation to a basic copper propionate [50] during cooling, after coming into contact with atmospheric air. The volatiles consist of CO_2, acetaldehyde and propionic acid. Finally, the product at 500°C consists of Cu and Cu_2O (Fig. 5a), and a significant 3% of carbon residues (Table 1, **D'**). This is probably due to the very inert local atmosphere when compared to the film (experiment **D**). This was also observed for other copper compounds (with long alkyl chains) in N_2 at 500°C [51].

In dry O_2 (C'), the reactive atmosphere displaces decomposition to lower temperature (Fig. 2a) but it does not impede Cu reduction (Supp. Info, Fig. S8). In fact, the final abrupt mass-loss step observed at 250ºC in the TG curve (and sharp exothermic peak in the DSC curve) is a clear signature of combustion, and in such a fast reaction mode complete oxidation is usually not possible [52]. After combustion, the sample mass reaches a minimum below the expected mass for the formation of CuO, but the subsequent mass increase (and the final black color) shows that it is then oxidized again to the expected CuO final product.

3.4 Thermal decomposition of $CuProp_2$ in film and powder at low pressure

At low pressure (experiment **E**), volatilization of the film occurs: the substrate is left with a blackish color, consistent with both copper oxide residues and elemental carbon, but the mass loss is close to 99%, and XRD analysis could not detect anything. A blue compound is found on the cold parts of the quartz tube which by FTIR and XRD analysis (Fig. S6) is revealed to be similar to $Cu(II)Prop_2$. Volatilization of $Cu(II)Prop_2$ occurs simultaneously with decomposition, since EGA-MS (Fig. 7, **E**) detects a small amount of volatiles, mainly related to propionic acid (m/z=74, 45, 29, 28, 27). Volatilization of copper propanoate was already observed by [34] above 167°C in vacuum, and it is consistent with a series of findings, for example that volatile binuclear Copper(I) carboxylates are among the decomposition products of Cu(II) carboxylates [53], and with the general strong tendency of copper complexes of even longer chains to sublimate at low pressure [54,55].

On the other hand, when the powder is heated in vacuum to 500°C (**E',E''**), at 10-25°C/min instead of 5°C/min, the sample decomposes between 150 and 300°C, yielding Cu(0). However, the crucible is almost empty, while the sample chamber has turned pink. Unlike **E**, where no m/z=44 is detected, the main fragments coming from the gas species are m/z=29,28,27 (C_2H_x), 44 (CO_2) and 45 (COOH), which could be in agreement with propionic acid (m/z=29,28,27,45), acetaldehyde (m/z=29,44) and CO_2 found by TG-MS-FTIR experiments (Fig. 4, **D'**). In **E'**, the first peak at 240°C follows scheme **α** and is due to residual water, as the water signal points inward (m/z=18). The CO_2 peak at 260°C is due to copper oxide's reduction to Cu(0) by elemental carbon, just like in **D**. Increasing mass and heating rate in **E''**, decomposition proceeds according to **γ** as in **D'**. Thus, **E'-E''** can be the consequence of pushing experiment **D-D'** to very low O_2 partial pressures, where only metallic copper is formed.

3.5 Thermochemistry calculations

As a further confirmation of the reactions proposed in Table 2, the experimental enthalpies of reaction for film and powder decomposition obtained from DSC (Fig. 2b) were compared with the theoretical values (Supp. Info) of electronic energy for the same reactions.

Hydrolysis (**α**) is predicted to be slightly endothermic, as observed for stage I in all experiments in film (**A**, **B**, **C**, **D**). This assignation is especially significant for the experiments in nominally dry atmosphere (**C** - O_2 and **D** - N_2), because it leads to the conclusion that residual humidity is enough to sustain this reaction.

Oxidation of the organic ligand (**β**) is exothermic and can occur at different degrees: thus, stage II in films in O_2 (**A** – humid, **C** - dry) is attributed to oxidation to acetaldehyde (entry iii and *iv*, in agreement with the detected volatiles) and its exothermicity decreases from **C** to **A** to **B** (humid N_2) as the degree of oxidation goes from *iv*, to *iii* to *ii*. **D** (dry N_2) represents an intermediate situation between films in O_2 and powders in N_2, since only partial reduction to Cu_2O occurs as the residual propionate decomposes in Stage II (**γ**). The latter (slightly endothermic) triggers the reduction of the CuO formed from stage I at the expenses of a stronger oxidation of the remaining organic ligand (probably to CO_2 and H_2O, see Fig. S7) according to *viii-x* (slightly exothermic), and combined they could explain why stage II is not accompanied by a relevant DSC peak (Fig.2b).

Concerning powder in N_2 (**D'**), the predicted slight endothermic character of the reduction reaction (*vi* of **γ**) is confirmed by experiment. In dry O_2 (**C'**), the heat evolved is lower than in films (**A**, **C**) indicating a lower degree of ligand oxidation (**β**) due to local O_2 depletion as reaction gases evolve [52], and as **γ** compete with **β**. This fact does not impede combustion occurring at the end of decomposition because, in contrast with the good thermal contact with the substrate for films, heat dissipation is much less efficient for powder [52].

4. Discussion

$CuProp_2$ decomposition kinetics depends on the geometry (film or powder) and the furnace atmosphere. A humid atmosphere triggers decomposition at lower temperature (Fig. 2) in films, promoting the hydrolysis (**α**) of the salt, and this shift is helped by reduced thickness. Films are so sensitive to humidity that the residual water vapor in nominally dry conditions (**C** and **D**) has a similar effect. Conversely, sensitivity to residual humidity or O_2 is lost for powders, which decompose at a much higher temperature. In fact, in bulk form, attention has to be paid to the local atmosphere created at the interparticle voids during decomposition [9,56,57]. This phenomenon results in inert or even reducing local conditions leading to similar behavior for powders in N_2 and in O_2: Cu(II) reduction (path **γ**) even in nominally pure O_2 (**C'**), and to a higher difficulty for carbon removal (Supp.Info, Fig. S8). Anyway, the nominal atmosphere has an effect on the decomposition process: combustion occurs in pure O_2. The difference in behavior between films and powders found for the particular case of $CuProp_2$, agrees with that of other metal organic salts [56].

Changing atmosphere affects the final product (Cu versus CuO) rather than the nature of the volatiles coming from decomposition (as in the case of $YProp_3$ [9]), which in both inert and oxidizing atmosphere consist of oxidized forms of the ligand. While in O_2 this is clearly understood from the high availability of oxygen, in inert atmosphere it can be explained by the oxidation of gaseous products contributing to the metal center reduction from Cu(II) to Cu(I) and Cu(0) according to reaction scheme **γ**. In fact, step II in **D** is more delayed than **B** due to decreasing oxygen availability (as H_2O vapor), but oxidation of residual ligand to CO_2 can still be pushed by the CuO/Cu_2O reduction.

This is in agreement with the hypothesis that [27], in inert conditions, metal ions that easily undergo redox reactions, like Cu, Ag and Hg, promote the formation of the corresponding carboxylate acid, while the evolution of ketones is favored by the opposite class of metals (i.e. Y, Ca..), emphasizing the role of the metal ion in affecting the salt decomposition. This would explain

why metal carboxylates that would normally release ketones, yield an acid in the presence of iron or copper salts [23,58].

No alkene was found, unlike for the decomposition of even chain Cu/Hg carboxylate [24,25], suggesting that the chain length may also play a role in the decomposition pathway or that the decomposition mechanism is a result of the general catalytic activity of copper, resulting in the oxidation of ethylene to acetaldehyde [59].

Lastly, reducing the pressure from atmospheric to 10^{-6} bar causes volatilization of the salt to occur, but at different stages of decomposition, according to the geometry of the sample and heating rate: the higher the surface to volume ratio (films, **E**), the faster the volatilization with respect to decomposition; conversely, at higher heating rates and thicker samples (**E''**), decomposition is more significant than volatilization. On the other hand, at atmospheric pressure, as the mass loss is never below than that of the expected compounds, any significant volatilization of copper species can be ruled out, until tested thicknesses of 300 nm. Additionally, the presence of water vapor is expected to prevent volatilization by shifting decomposition to low temperatures thanks to scheme **α**. Indeed, the hydrolysis-driven decomposition of the carboxylate salts, already also found for the $YProp_3$ case [9], can explain the advantage of using humid atmospheres in the framework of CSD-YBCO film pyrolysis; in fact, humidity is critical to reduce the decomposition temperatures of the thermal treatment.

5. Conclusions

In conclusion, the thermal decomposition of $CuProp_2$ was studied for samples in the form of powder and as film. By IR and MS detection of the volatiles, we were able to identify almost univocally the species evolved during decomposition (dominated by propionic acid), clarifying the mechanism with respect to the literature. While, as a consequence of the chemical nature of the metal center, the nature of the volatiles does not vary in response to the atmosphere change or in relation to the surface to volume ratio of the sample, the CuO-Cu redox behavior is found to be affected by it. Specifically, it is easier to obtain Cu_2O and Cu from powders than from films. Additionally, the comparison of experimental and computational thermochemistry data helped clarify and support the decomposition reactions written based on the observed volatiles. Finally, the role of water vapor in the pyrolysis of YBCO films has been cleared. Humidity promotes decomposition at low temperatures, where volatilization would otherwise prevail in a low-pressure environment. Therefore, the study of films' thermal behavior is not only crucial for identifying the intrinsic thermal mechanisms that could pass unnoticed while studying powders, but also for the analysis of the real phenomena occurring during tape synthesis of high temperature superconductors and other functional oxide films.

Acknowledgments

This work was supported by the Spanish Programa Nacional de Materiales through the COACHSUPENERGY project (grant numbers MAT2014-51778-C2-1-R and MAT2014-51778-C2-2-R, co-financed by the European Regional Development Fund), by the Center of Excellence Severo Ochoa (SEV-2015-0496), the Generalitat of Catalunya (SGR753 and SGR948) and by the *Universitat de Girona* (UdG, contract No. MPCUdG2016/059). SR and FS thanks the University of Girona (UdG) and the Cardiff University School of Chemistry, respectively, for their fully-funded PhD scholarships. The authors also wish to thank the Scientific services of the UdG and the Institute of Materials Science of Barcelona (ICMAB). Computing facilities were provided by ARCCA at Cardiff

University, HPC Wales, and through the membership of the UK's Materials Chemistry Consortium (MCC), which is funded by EPSRC (EP/F067496).

References

[1] H. Maeda, Y. Yanagisawa, Recent Developments in High-Temperature Superconducting Magnet Technology (Review), IEEE Trans. Appl. Supercond. 24 (2014) 1–12. doi:10.1109/TASC.2013.2287707.

[2] X. Obradors, T. Puig, Coated conductors for power applications: materials challenges, Supercond. Sci. Technol. 27 (2014) 44003–44019. doi:10.1088/0953-2048/27/4/044003.

[3] T. Schneller, R. Waser, M. Kosec, D. Payne, Chemical Solution Deposition of Functional Oxide Thin Films, Springer, 2013. doi:10.1007/978-3-211-99311-8.

[4] X. Obradors, T. Puig, M. Gibert, A. Queraltó, J. Zabaleta, N. Mestres, Chemical solution route to self-assembled epitaxial oxide nanostructures, Chem. Soc. Rev. 43 (2014) 2200–2225. doi:10.1039/c3cs60365b.

[5] P. Vermeir, I. Cardinael, J. Schaubroeck, K. Verbeken, B. Michael, P. Lommens, W. Knaepen, D. Jan, K. De Buysser, I. Van Driessche, Elucidation of the Mechanism in Fluorine-Free Prepared YBa2Cu3O7-δ Coatings, Inorg. Chem. 49 (2010) 4471–4477. doi:10.1021/ic9021799.

[6] J. Farjas, J. Camps, P. Roura, S. Ricart, T. Puig, X. Obradors, Thermoanalytical study of the formation mechanism of yttria from yttrium acetate, Thermochim. Acta. 521 (2011) 84–89. doi:10.1016/j.tca.2011.04.009.

[7] J.-C.C. Grivel, Thermal decomposition of yttrium(III) propionate and butyrate, J. Anal. Appl. Pyrolysis. 101 (2013) 185–192. doi:10.1016/j.jaap.2013.01.011.

[8] M. Nasui, C. Bogatan (Pop), L. Ciontea, T. Petrisor, Synthesis, crystal structure modeling and thermal decomposition of yttrium propionate [Y2(CH3CH2COO)6·H2O]·3.5H2O, J. Anal. Appl. Pyrolysis. 97 (2012) 88–93. doi:10.1016/j.jaap.2012.05.003.

[9] S. Rasi, S. Ricart, X. Obradors, T. Puig, P. Roura, J. Farjas, Thermal decomposition of yttrium propionate: film and powder, J. Anal. Appl. Pyrolysis. (2018). doi:10.1016/j.jaap.2018.03.021.

[10] Z. Lin, D. Han, S. Li, Study on thermal decomposition of copper(II) acetate monohydrate in air, J. Therm. Anal. Calorim. 107 (2012) 471–475. doi:10.1007/s10973-011-1454-4.

[11] M. Nasui, R.B. Mos, T. Petrisor Jr, M.S. Gabor, R.A. Varga, L. Ciontea, T. Petrisor, Synthesis, crystal structure and thermal decomposition of a new copper propionate [Cu(CH3CH2COO)2]·2H2O, J. Anal. Appl. Pyrolysis. 92 (2011) 439–444. doi:10.1016/j.jaap.2011.08.005.

[12] M.D. Judd, B.A. Plunkett, M.I. Pope, The thermal decomposition of calcium, sodium, silver and copper(II) acetates, J. Therm. Anal. 6 (1974) 555–563. doi:10.1007/BF01911560.

[13] J.A. Hill, C.B. Murphy, G.P. Schacher, Observations on the thermal decomposition of cupric acetate monohydrate, Anal. Chim. Acta. 24 (1961) 496–497. doi:10.1016/0003-2670(61)80103-7.

[14] K.C. Patil, G. V Chandrashekhar, M. V George, C.N.R. Rao, Infrared spectra and thermal decompositions of metal acetates and dicarboxylates, Can. J. Chem. 46 (1968) 257–265. doi:10.1139/v68-040.

[15] P.S. Bassi, H.S. Jamwal, B.S. Randhawa, Comparative study of the thermal analyses of some transition metal(II) propionates. Part I, Thermochim. Acta. 71 (1983) 15–24.

doi:10.1016/0040-6031(83)80351-7.
[16] L.D.S. Mindrale, U.C. Bernard--, Comportement Thermique des Propionates Hydrates de Calcium, Strontium et Baryum, J. Therm. Anal. 12 (1977) 33–42. doi:10.1007/bf01909853.
[17] R.B. Mos, M. Nasui, T. Petrisor Jr, M.S. Gabor, R. Varga, L. Ciontea, T. Petrisor, Synthesis, crystal structure and thermal decomposition study of a new barium acetato-propionate complex, J. Anal. Appl. Pyrolysis. 92 (2011) 445–449. doi:10.1016/j.jaap.2011.08.007.
[18] J. Mu, D.D. Perlmutter, Thermal decomposition of carbonates, carboxylates, oxalates, acetates, formates and hydroxides, Thermochim. Acta. 49 (1981) 207–218. doi:10.1016/0040-6031(81)80175-X.
[19] P.C. Kalsi, P.S. Bassi, C.M. Khajuria, Kinetics of the isothermal decomposition of Cu(II) Butyrate, Termochimica Acta. 41 (1980) 265–268. doi:10.1016/0040-6031(80)80074-8.
[20] J. Grivel, Thermal decomposition of yttrium(III) propionate and butyrate, J. Anal. Appl. Pyrolysis. 101 (2013) 185–192. doi:10.1016/j.jaap.2013.01.011.
[21] J. Grivel, Thermal decomposition of lutetium propionate, J. Anal. Appl. Pyrolysis. 89 (2010) 250–254. doi:10.1016/j.jaap.2010.08.011.
[22] J. Grivel, Thermal decomposition of Ln(C2H5CO2)3•H2O (Ln=Ho,Er,Tm and Yb), J. Therm. Anal. Calorim. 109 (2012) 81–88. doi:10.1007/s10973-011-1745-9.
[23] R.A. Hites, K. Biemann, On the Mechanism of Ketonic Decarboxylation. Pyrolysis of Calcium Decanoate, J. Am. Chem. Soc. 94 (1972) 5772–5777. doi:10.1021/ja00771a039.
[24] M.S. Akanni, O.B. Ajayi, J.N. Lambi, Pyrolytic Decomposition of Some Even Chain Length Copper(II) Carboxylates, J. Therm. Anal. 31 (1986) 131–143. doi:10.1007/bf01913894.
[25] M.S. Akanni, H.D. Burrows, P.B. Begun, Product analysis, reaction mechanism and kinetics of the thermal decomposition of some even chain-length mercury(II) carboxylates, Termochimica Acta. 81 (1984) 45–58. doi:10.1016/0040-6031(84)85109-6.
[26] R. Szczęsny, E. Szlyk, Thermal decomposition of some silver (I) carboxylates under nitrogen atmosphere, J. Therm. Anal. Calorim. 111 (2013) 1325–1330. doi:10.1007/s10973-012-2485-1.
[27] M.S. Akanni, E.K. Okoh, H.D. Burrows, H.A. Ellis, The thermal behaviour of divalent and higher valent metal soaps : a review, Thermochim. Acta. 208 (1992) 1–41. doi:10.1016/0040-6031(92)80150-u.
[28] X. Palmer, C. Pop, H. Eloussi, B. Villarejo, P. Roura, J. Farjas, A. Calleja, A. Palau, T. Puig, S. Ricart, Solution design for low-fluorine trifluoroacetate route to YBa2Cu3O7 films, Supercond. Sci. Technol. 29 (2016) 24002. doi:10.1088/0953-2048/29/2/024002.
[29] O.C. Bridgeman, E.W. Aldrich, Vapor Pressure Tables for Water, J. Heat Transfer. 86 (1964) 279. doi:10.1115/1.3687121.
[30] L. Nattermann, O. Maßmeyer, E. Sterzer, V. Derpmann, H.Y. Chung, W. Stolz, K. Volz, An experimental approach for real time mass spectrometric CVD gas phase investigations, Sci. Rep. 8 (2018) 1–7. doi:10.1038/s41598-017-18662-7.
[31] R.M. Reese, V.H. Dibeler, F.L. Mohler, Temperature Variation of Mass Spectra of Hydrocarbons, J. Res. Natl. Bur. Stand. (1934). 46 (1951) 79–84. doi:10.6028/jres.046.012.
[32] G. Kresse, J. Hafner, Ab initiomolecular dynamics for liquid metals, Phys. Rev. B. 47 (1993) 558–561. doi:10.1103/physrevb.47.558.
[33] G. Kresse, J. Furthmüller, Efficiency of ab-initio total energy calculations for metals and semiconductors using a plane-wave basis set, Comput. Mater. Sci. 6 (1996) 15–50. doi:10.1016/0927-0256(96)00008-0.
[34] J.A.R. Cheda, M. V García, M.I. Redondo, S. Gargani, P. Ferloni, Short chain copper(II) n-alkanoate liquid crystals, Liq. Cryst. 31 (2004) 1–14. doi:10.1080/02678290310001628500.
[35] Y.H. Chung, H.H. Wei, Y.H. Liu, G.H. Lee, Y. Wang, Reinvestigation of the crystal structure

and cryomagnetic behaviour of copper(II) propionates, Polyhedron. 17 (1998) 449–455. doi:10.1016/s0277-5387(97)00367-7.
[36] B. Kozlevčar, P. Šegedin, Structural Analysis of a Series of Copper (II) Coordination Compounds and Correlation with their Magnetic Properties, in: Croat. Chem. Acta, 2008: pp. 369–379.
[37] A. Elmali, The Magnetic Super-Exchange Coupling in Copper (II) Acetate Monohydrate and a Redetermination of the Crystal Structure, Turk J Phy. 24 (2000) 667–672.
[38] X. Rocquefelte, K. Schwarz, P. Blaha, Theoretical Investigation of the Magnetic Exchange Interactions in Copper (II) Oxides under Chemical and Physical Pressures, 2012. doi:10.1038/srep00759.
[39] R.L. Martin, H. Waterman, Magnetic Studies with Copper(II) Salts. Part II. Anomalous Paramagnetism and ð-Bonding in Anhydrous and Hydrated Copper(II) n-Alkanoeates., J. Chem. Soc. (1957) 2545–2551. doi:10.1039/JR9570002545.
[40] V.V. Zelentsov, Magnetic susceptibility of some copper(II) carboxylates, J. Struct. Chem. 6 (1966) 819–823. doi:10.1007/bf00747102.
[41] I.A. Martynova, D.M. Tsymbarenko, N.P. Kuz'mina, Yttrium Tris Propionate Monohydrate : Synthesis , Crystal Structure , and Thermal Stability, Russ. J. Coord. Chem. 40 (2014) 565–570. doi:10.1134/S1070328414080077.
[42] M. Kakihana, T. Nagumo, Assignment for the Infrared Spectrum of Solid Sodium Propionate from Low-Temperature Measurements in Combination with 13C Isotopic Shifts, Zeitschrift Für Naturforsch. A. 42 (1987) 477–484. doi:10.1515/zna-1987-0509.
[43] R. Urlaub, U. Posset, R. Thull, FT-IR spectroscopic investigations on sol—gel-derived coatings from acid-modified titanium alkoxides, J. Non-Cyrstalline Solids. 265 (2000) 276–284. doi:10.1016/s0022-3093(00)00003-x.
[44] S. Doeuff, M. Henry, C. Sanchez, J. Livage, Hydrolysis of titanium alkoxides: modification of the molecular precursor by acetic acid, J. Non-Cyrstalline Solids. 9 (1987) 206–216. doi:10.1016/s0022-3093(87)80333-2.
[45] W.J. Newton, C. Oldham, B.J. Tabner, Magnetic Susceptibility and Electron Spin Resonance of Some Copper(II) Unsaturated Carboxylates, Chem. Informationsd. 11 (1980) 1379–1382. doi:10.1002/chin.198046063.
[46] H. Henmi, T. Hirayama, N. Mizutani, M. Kato, Thermal decomposition of basic copper carbonate, CuCO3•Cu(OH)2·H2O, in carbon dioxide atmosphere (0-50 atm), Thermochim. Acta. 96 (1985) 145–153. doi:10.1016/0040-6031(85)80017-4.
[47] M. Estruga, A. Roig, C. Domingo, J.A. Ayllón, Solution-processable carboxylate-capped CuO nanoparticles obtained by a simple solventless method, J. Nanopart. Res. 14 (2012) 1053–8. doi:10.1007/s11051-012-1053-8.
[48] D. Mott, J. Galkowski, L. Wang, J. Luo, C. Zhong, Synthesis of Size-Controlled and Shaped Copper Nanoparticles, Langmuir. 23 (2007) 5740–5745. doi:10.1021/la0635092.
[49] M.A. Ben Aissa, B. Tremblay, A. Andrieux-Ledier, E. Maisonhaute, N. Raouafi, A. Courty, Copper nanoparticles of well-controlled size and shape: a new advance in synthesis and self-organization, Nanoscale. 7 (2015) 3189–3195. doi:10.1039/c4nr06893a.
[50] A. Echavarría, F. Echeverría, C. Arroyave, H. Gil, Study of the Copper Corrosion Mechanism in the Presence of Propionic Acid Vapors, J. Braz. Chem. Soc. 20 (2009) 1841–1848. doi:10.1590/s0103-50532009001000011.
[51] D. Deng, T. Qi, Y. Cheng, Y. Jin, F. Xiao, Copper carboxylate with different carbon chain lengths as metal–organic decomposition ink, J. Mater. Sci Mater Electron. 25 (2014) 390–397. doi:10.1007/s10854-013-1599-y.
[52] D. Sánchez-Rodriguez, J. Farjas, P. Roura, The critical conditions for thermal explosion in a

system heated at a constant rate, Combust. Flame. 18 (2017) 211–219. doi:10.1016/j.combustflame.2017.08.008.
[53] C. Reichert, D.K.C. Fung, D.C.K. Lin, J.B. Westmore, Thermal Decomposition of Copper (II) Carboxylates: Mass Spectra of Binuclear Copper(I) Carboxilates, Chem. Commun. (1968) 1094. doi:10.1039/c19680001094.
[54] Y. Pauleau, A.Y. Fasasi, Kinetics of Sublimation of Copper(II) Acetylacetonate Complex Used for Chemical Vapor Deposition of Copper Film, Chem. Mater. 3 (1991) 45–50. doi:10.1021/cm00013a015.
[55] F. KÖSY, A Volatile Compound of Copper, Nature. 160 (1947) 21. doi:10.1038/160021a0.
[56] P. Roura, J. Farjas, H. Eloussi, L. Carreras, S. Ricart, T. Puig, X. Obradors, Thermal analysis of metal organic precursors for functional oxide preparation: Thin films versus powders, Thermochim. Acta. 601 (2015) 1–8. doi:10.1016/j.tca.2014.12.016.
[57] P. Roura, J. Farjas, J. Camps, S. Ricart, J. Arbiol, T. Puig, X. Obradors, Decomposition processes and structural transformations of cerium propionate into nanocrystalline ceria at different oxygen partial pressures, J. Nanopart. Res. 13 (2011) 4085–4096. doi:10.1007/s11051-011-0352-9.
[58] J.J. Duruz, H.J. Michels, A.R. Ubbelohde, Decomposition Reactions of Sodium Propionate, J. Che. (1971) 1505–1509. doi:10.1039/j29710001505.
[59] D. Torres, N. Lopez, F. Illas, R.M. Lambert, Why Copper Is Intrinsically More Selective than Silver in Alkene Epoxidation : Ethylene Oxidation on Cu (111) versus Ag (111), J. Am. Chem. Soc. 127 (2005) 10774–10775. doi:10.1021/ja043227t.
[60] W.E. Wallace, Infrared Spectra, in: P.J. Linstrom, W.G. Mallard (Eds.), NIST Chem. WebBook, NIST Stand. Ref. Database Number 69, Institute of Standards and Technology, Gaithersburg MD, 20899, n.d. doi:https://doi.org/10.18434/T4D303.
[61] W.E. Wallace, Mass spectra, in: P.J. Linstrom, W.G. Mallard (Eds.), NIST Chem. WebBook, NIST Stand. Ref. Database Number 69, National Institute of Standards and Technology, Gaithersburg MD, 20899, n.d. doi:https://doi.org/10.18434/T4D303.

Figure captions

Fig. 1: IR and XRD (inset) spectra of $CuProp_2$ as film after drying. FTIR assignments according to [34].

Fig. 2: (a) TG curves showing the influence of atmosphere and sample layout on the decomposition of $CuProp_2$ at 5K/min for ~2-µm films and 27-mg powders; (b) corresponding DSC signal normalized by the initial sample mass (m_i). For a quantitative DSC analysis, see Table 2. Experiments were run until 500°C, but only temperatures where mass or DSC changes occur are shown.

Fig. 3: FTIR spectra representing the gases evolved at the decomposition peak temperatures during powder and film pyrolysis (see Fig. 2). Although the spectra are normalized by the $CuProp_2$ moles involved in the mass-loss step (n_I, n_{II} for films, n_i for powders), quantitative comparisons should be done carefully, taking into account that the intensity may not be directly proportional to the sample amount. FTIR assignment based on [60]. The detailed evolution of each volatile is reported in Fig. 4.

Fig. 4: TG-EGA of $CuProp_2$ decomposition at 5K/min as film and as powder in different atmospheres. The frequencies shown for each volatile are: 1780 cm^{-1} (C=O) for propionic acid, 2355 cm^{-1} for CO_2, 2741 cm^{-1} (CH) for acetaldehyde; as in Fig. 3, the transmittance was normalized by the Cu moles responsible for the IR signal at each step, to give a more realistic idea of the relative importance of a volatile. m/z=44 was also detected in **D'** but is not shown for clarity.

Fig. 5: XRD analysis of (a) final products at 500°C and (b) quenched samples at different temperatures as a function of the atmosphere. (•) $CuProp_2$; (△) unknown phase. The silicon peak corresponds to the sample holder.

Fig. 6: Infrared evolution of the solid residue during decomposition of $CuProp_2$ as film and powder in different atmospheres. Details of the COO^- stretching region can be found in the Supp. Info. (•) $CuProp_2$; (△) unknown phase. The vertical lines are drawn to show that ν_{as} gets closer to ν_s as pyrolysis proceeds.

Fig. 7: EGA-MS of $CuProp_2$ decomposition in vacuum as film on LAO at 5K/min (**E**) and as powder at 10K/min (**E'**) and 25K/min (**E'**). Note that the amount of powder in **E'** is not enough for the decomposition to follow only reaction scheme **γ** and so its behavior is similar to **D**. On the other hand, **E''** behaves like **D'**. Mass spectra assignment based on [61].

Tables

Compound	Found (Expected), mass %	
	%C	%H
$CuProp_2$	33.71 (34.37)	4.29 (4.81)
A (Film, hum O_2, 210°C)	4.70	0.38
A (Film, hum O_2, 500°C)	-	-
D (Film, dry N_2, 230°C)	4.85	1.32
D (Film, dry N_2, 500°C)	-	-
D' (Powder, dry N_2, 500°C)	3.56	-

Table 1: Weight percentages determined from Elemental Analysis of initial and final products. (-) values inferior to detection limits.

	Reaction scheme	**Reaction**	$\Delta_r E$ **(VASP/PBE)** *[Kcal/mol)*	$\Delta_r H$ **exp.** *[Kcal/mol)*
i	$CuProp_2 + H_2O \rightarrow CuO + 2C_2H_5CO_2H$	Hydrolysis (**α**)	22.1	19 (**A**, film, Stage I) 12 (**B**, film Stage I) 17 (**C**, film, Stage I) 18 (**D**, Stage I)
ii	$CuProp_2 + O_2 \rightarrow CH_3CHO + C_2H_5CO_2H + CO_2 + CuO$	Oxidation (**β**)	-49.5	-80 (**B**, film, Stage II)
iii	$CuProp_2 + 2O_2 \rightarrow 2CH_3CHO + H_2O + 2CO_2 + CuO$		-121.1	-240 (**A**, film, Stage II)
iv	$CuProp_2 + 9/2O_2 \rightarrow CH_3CHO + 3H_2O + 4CO_2 + CuO$		-364.5	-380 (**C**, film Stage II) -170 (**C'**, powder, O_2)
v	$CuProp_2 + 7O_2 \rightarrow 6CO_2 + 5H_2O + CuO$	Full oxidation	-607.9	
vi	$CuProp_2 \rightarrow CO + CH_3CHO + C_2H_5CO_2H + Cu$	Reduction (**γ**)	48.6	19 (**D'**, powder, N_2)
vii	$CO + ½O_2 \rightarrow CO_2$		(-67.6*)	33 (powder, Ar)
viii	$2CO \rightarrow C + CO_2$		(-41.2*)	
ix	$C + O_2 \rightarrow CO_2$		(-94.0*)	
x	$CuO + ¼\ C \rightarrow ½\ Cu_2O + ¼CO_2$		(-6.1*)	<0 (**D**, film Stage II)

*Table 2: Experimental enthalpy of decomposition ($\Delta_r H$ exp) and calculated electronic energy of reaction ($\Delta_r E$) for possible decomposition paths of $CuProp_2$. (+) for endothermic reactions and (-) for exothermic reactions. *literature values of $\Delta_r H$ are given in brackets; experimental values are normalized by the $CuProp_2$ mass that decomposes at the DSC step, which is calculated from TG curves (more details in Supp. Info.) Comparison with the theoretical values is meant to show which reaction scheme contributes the most to decomposition (See section 3.5).*

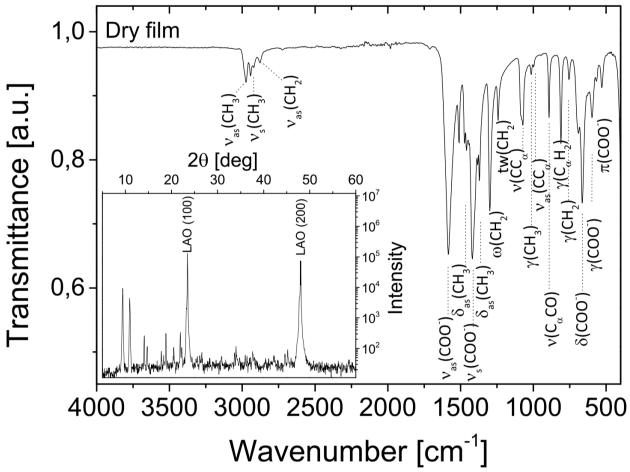
Dry film
Transmittance [a.u.]
1,0
0,8
0,6
Wavenumber [cm-1]
4000 3500 3000 2500 2000 1500 1000 500
2θ [deg]
10 20 30 40 50 60
LAO (100)
LAO (200)
Intensity
νas(CH3)
νs(CH3)
νas(CH2)
νas(COO)
νs(COO)
δas(CH3)
δas(CH3)
ω(CH2)
tw(CH2)
ν(Cα-C)
γ(CH3)
ν(Cα-CO)
νas(Cα-C)
γ(Cα-H2)
γ(CH2)
δ(COO)
γ(COO)
π(COO)

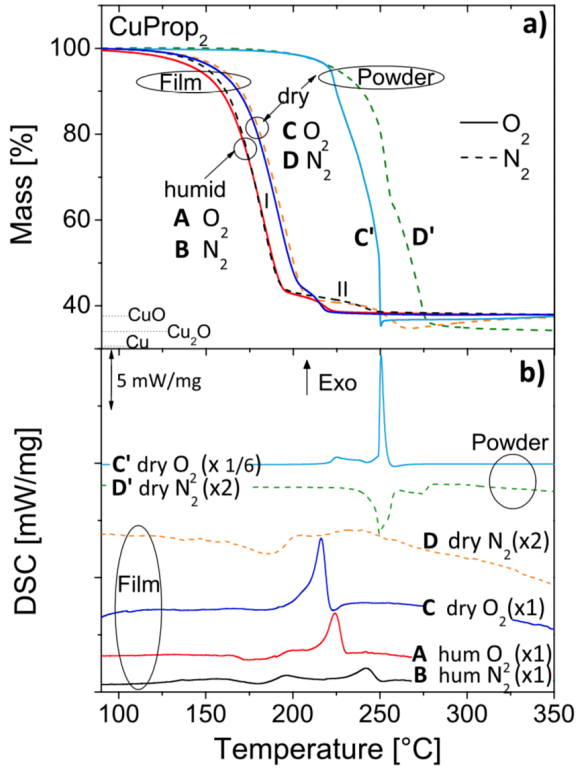
CuProp2
a)
Mass [%]
100
80
60
40
Film
Powder
dry
C O2
D N2
humid
A O2
B N2
I
II
C'
D'
O2
N2
CuO
Cu2O
Cu
b)
5 mW/mg
Exo
DSC [mW/mg]
C' dry O2 (x 1/6)
D' dry N2 (x2)
Powder
D dry N2(x2)
Film
C dry O2(x1)
A hum O2 (x1)
B hum N2 (x1)
100 150 200 250 300 350
Temperature [°C]

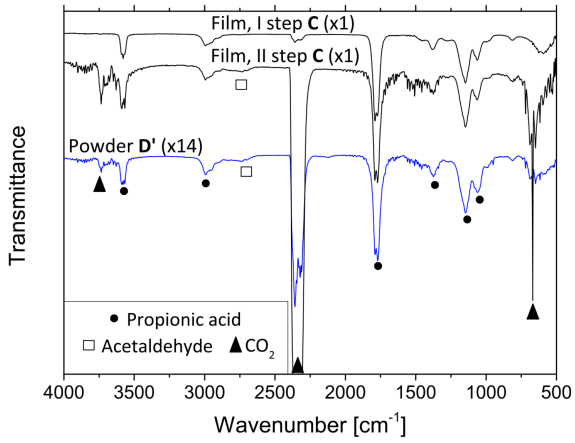
Film, I step C (x1)
Film, II step C (x1)
Powder D' (x14)
Transmittance
Propionic acid
Acetaldehyde
CO2
4000 3500 3000 2500 2000 1500 1000 500
Wavenumber [cm-1]

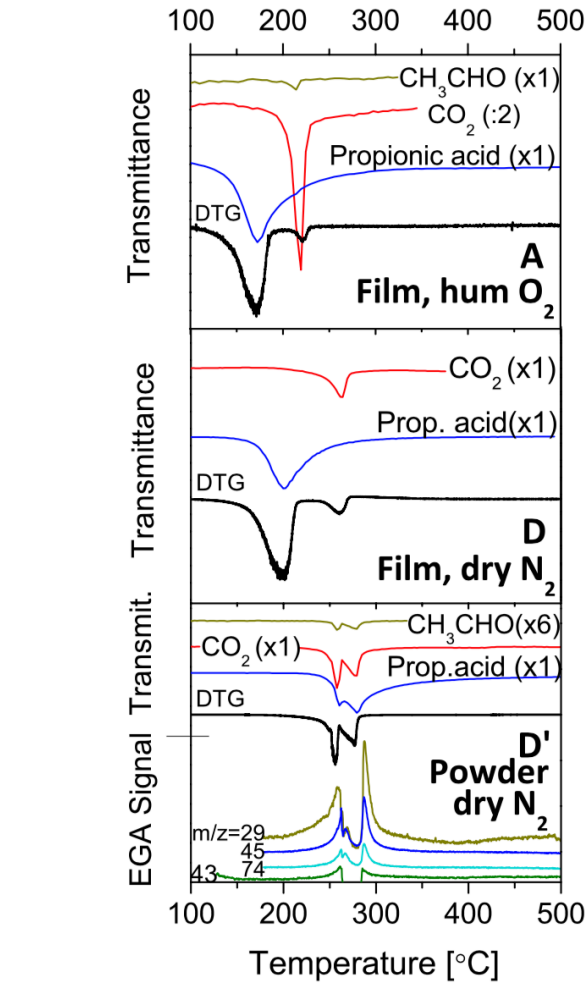
100
200
300
400
500
Transmittance
CH3CHO (x1)
CO2 (:2)
Propionic acid (x1)
DTG
A
Film, hum O2
Transmittance
CO2 (x1)
Prop. acid(x1)
DTG
D
Film, dry N2
Transmit.
CH3CHO(x6)
CO2 (x1)
Prop.acid (x1)
DTG
EGA Signal
D'
Powder
dry N2
m/z=29
45
43
74
Temperature [°C]

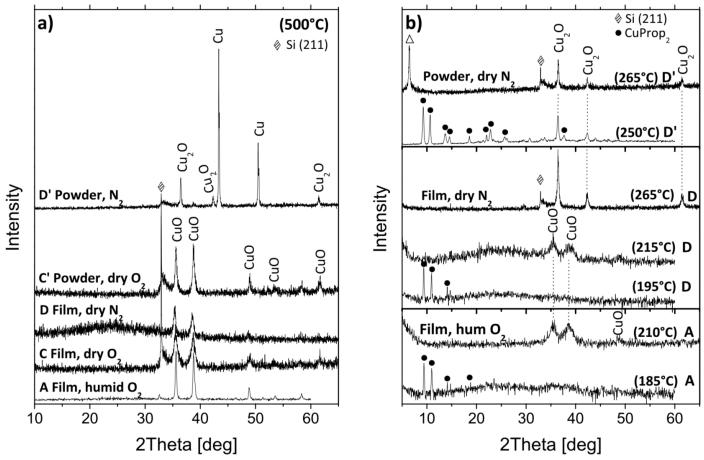
a)
(500°C)
Si (211)
Cu
Cu2O
CuO
D' Powder, N2
C' Powder, dry O2
D Film, dry N2
C Film, dry O2
A Film, humid O2
Intensity
2Theta [deg]
b)
Si (211)
CuProp2
Powder, dry N2
(265°C) D'
(250°C) D'
Film, dry N2
(265°C) D
(215°C) D
(195°C) D
Film, hum O2
(210°C) A
(185°C) A
Intensity
2Theta [deg]

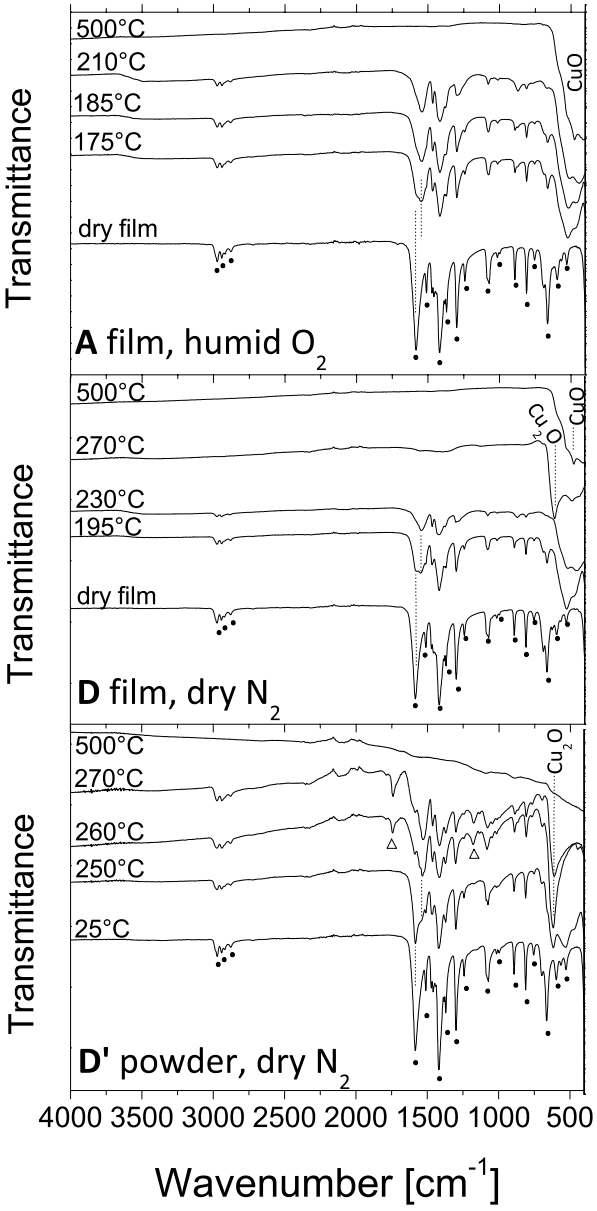
500°C
210°C
185°C
175°C
dry film
A film, humid O2
CuO
Transmittance
500°C
270°C
230°C
195°C
dry film
D film, dry N2
Cu2O
CuO
Transmittance
500°C
270°C
260°C
250°C
25°C
D' powder, dry N2
Cu2O
Transmittance
4000 3500 3000 2500 2000 1500 1000 500
Wavenumber [cm-1]

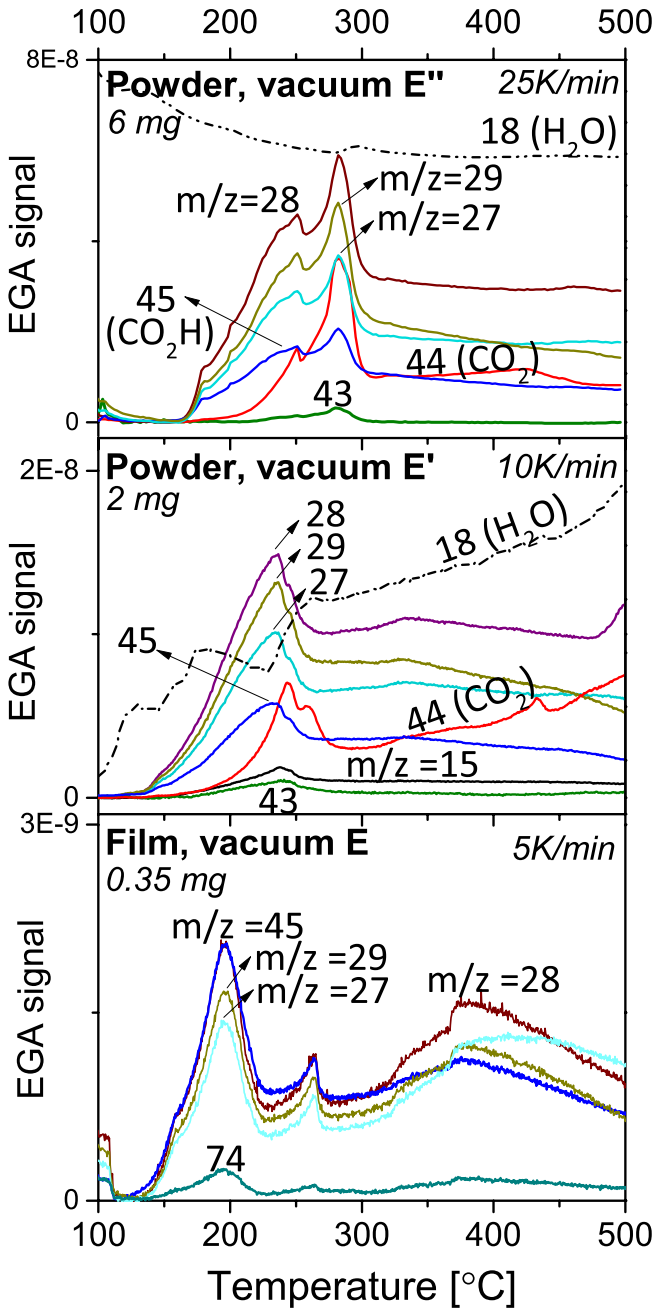
100
200
300
400
500
8E-8
Powder, vacuum E"
25K/min
6 mg
18 (H2O)
m/z=28
m/z=29
m/z=27
45
(CO2H)
44 (CO2)
43
EGA signal
0
2E-8
Powder, vacuum E'
10K/min
2 mg
28
29
27
18 (H2O)
45
44 (CO2)
m/z =15
43
EGA signal
0
3E-9
Film, vacuum E
5K/min
0.35 mg
m/z =45
m/z =29
m/z =27
m/z =28
74
EGA signal
0
100
200
300
400
500
Temperature [°C]

SUPPORTING INFORMATION

Thermal decomposition of $CuProp_2$: in-situ analysis of film and powder pyrolysis

Silvia Rasi, Fabrizio Silveri, Susagna Ricart, Xavier Obradors, Teresa Puig, Pere Roura and Jordi Farjas

Complementary characterization of initial product

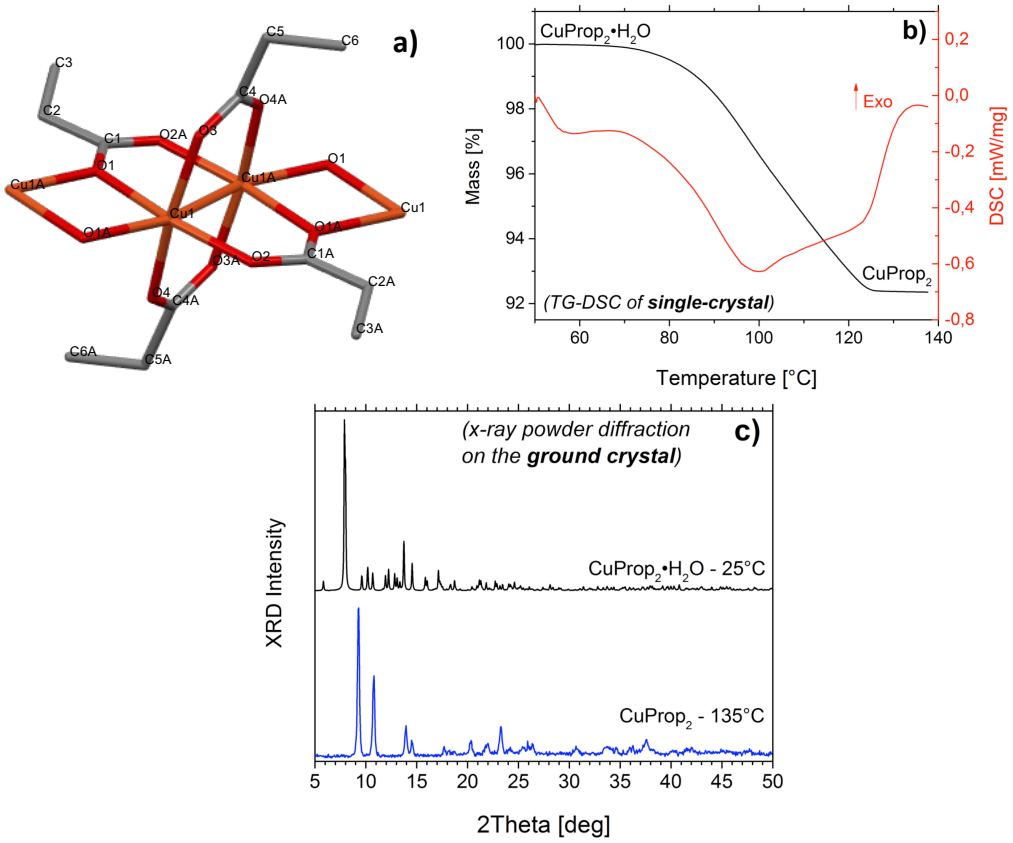

***Fig. S1**: **a)** single-crystal x-ray analysis performed on a crystal obtained from the solution of this study ($CuAc_2$ in propionic acid/meOH), showing the structure to be that of CCDC database code 1133510, belonging to the P-1 symmetry space group (triclinic) [S1]; **b)** TG/DSC of that single-crystal, showing an endothermic peak corresponding to 7.7% mass loss (approximately one H_2O molecule per Cu); this stage is not observed in films as they are dried before TG analysis. **c)** corresponding powder diffraction curves of the ground crystal before and after dehydration, which confirms the structure to be identical to that of the dry film (Fig. S2-b).*

[S1] Y.H.Chung, H.H.Wei, Y.H.Liu, G.H.Lee, Y.Wang, Polyhedron (1998) 17, 449-455. doi: 10.1016/S0277-5387(97)00367-7.

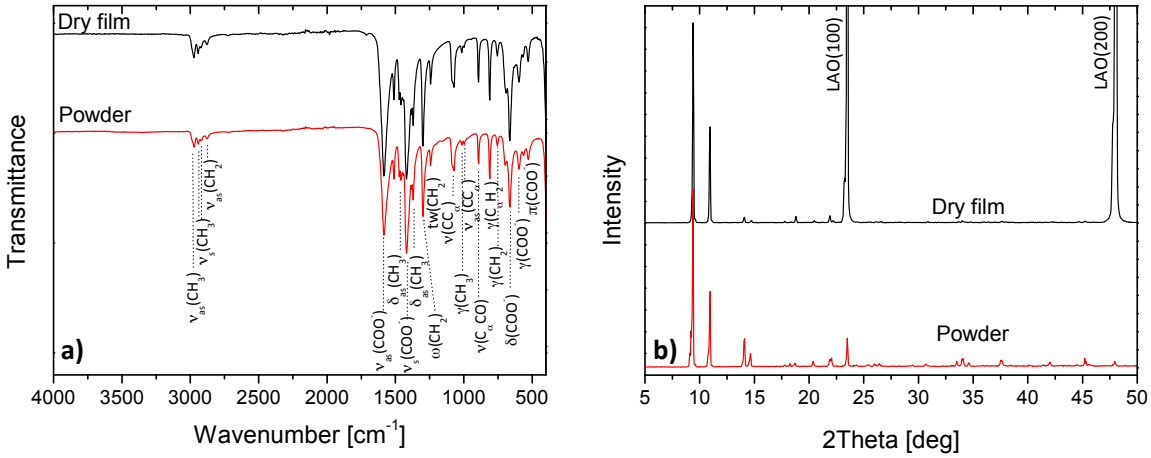

***Fig. S2**: (a) IR and (b) XRD spectra of $CuProp_2$ as film and powder.*

Compound	Found (Expected), mass %	
	%C	%H
$CuProp_2$:		
From $CuCO_3$	33.86 (34.37)	4.38 (4.81)
From $CuAc_2$	33.71 (34.37)	4.29 (4.81)

***Table. S1**: Comparison between $CuProp_2$ obtained from an acetate-free solution and the $CuProp_2$ obtained from the $CuAc_2$ solution used in the current work.*

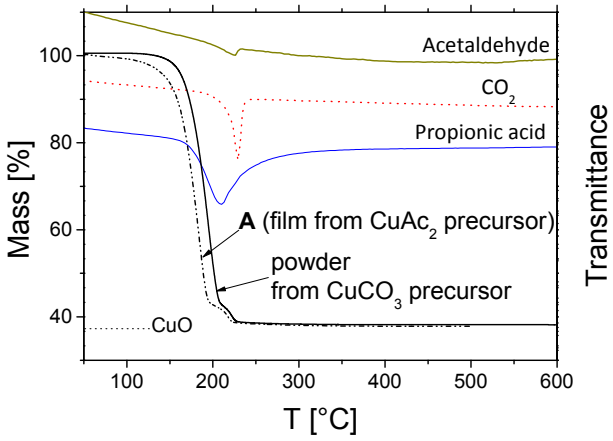

***Fig. S3**: Decomposition of the $CuProp_2$ powder obtained from an acetate-free solution in comparison with the film, **A**, from the $CuAc_2$ precursor. The powder (8 mg) was spread on LAO substrate to imitate film conditions, and heated up at 5K/min in humid O_2.*

Complementary characterization of decomposition products

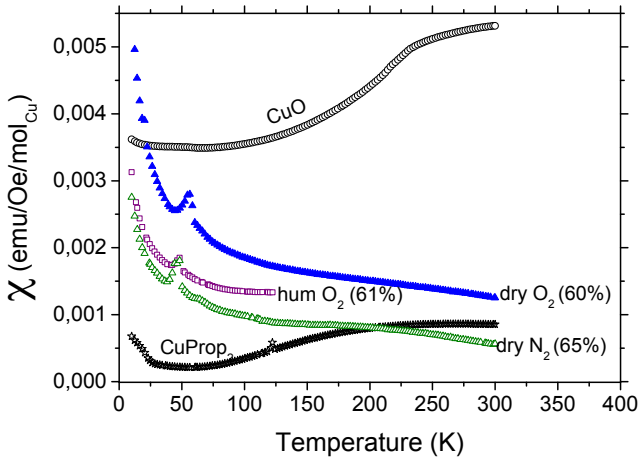

Fig. S4: *Molar susceptibility (χ) as a function of temperature for initial ($CuProp_2$) and final product (CuO) and for a film quenched at similar m_f/m_i (shown in brackets) in different atmospheres. χ molar of the quenches was calculated extrapolating the theoretical moles of copper from the % mass loss. The small peak between 50-55K can be attributed to O_2 traces on the sample surface during measurements, and it is independent of the sample properties.*

Magnetic measurements where performed with a Superconducting Quantum Interference Device (SQUID) Magnetometer from Quantum Design equipped with a superconducting magnet of 7 T. All measurements were performed in a magnetic field of 1000 Oe and corrected for the blank of the sample holder (diamagnetic gel capsule).

Cu(II) is a paramagnetic ion, however, the theoretical value for μ_{eff} from the spin-only approximation (1.73μ_B) and the experimental range from literature (1.9-2.2 μ_B) [S2,S3] for solutions of copper compounds differ from solid copper complexes where the binuclear structure creates antiferromagnetic interactions [S2,S3]. **Fig.S4** shows how, during decomposition, these antiferromagnetic interactions decrease with increasing paramagnetic Cu(II) contribution, although this contribution is never pure, probably because decomposition of the initial product is not yet completed.

The paramagnetic contribution of the magnetic susceptibility (χ) as a function of temperature can be fitted according to Curie's law, when there is direct proportionality between 1/χ and T through a constant slope (1/*C*), which can be used to calculate the magnetic moment (μ_{eff}):

$$\mu_{eff} = 2.828 \cdot \sqrt{C} \qquad \text{(in c.g.s. units)}$$

Values between 0.8-1.2 were found for the quenched samples shown in **Fig. S4**.

In the case of more complex behaviors (like $CuProp_2$ and CuO), other equations can be used to fit μ_{eff}, but this quantitative analysis was not carried out in the present work.

[S2] R.L. Martin, H. Waterman, J. Chem. Soc. (1957) 2545–2551. doi:10.1039/JR9570002545.
[S3] V.V. Zelentsov, J. Struct. Chem. 6 (1966) 819–823. doi:10.1007/bf00747102.

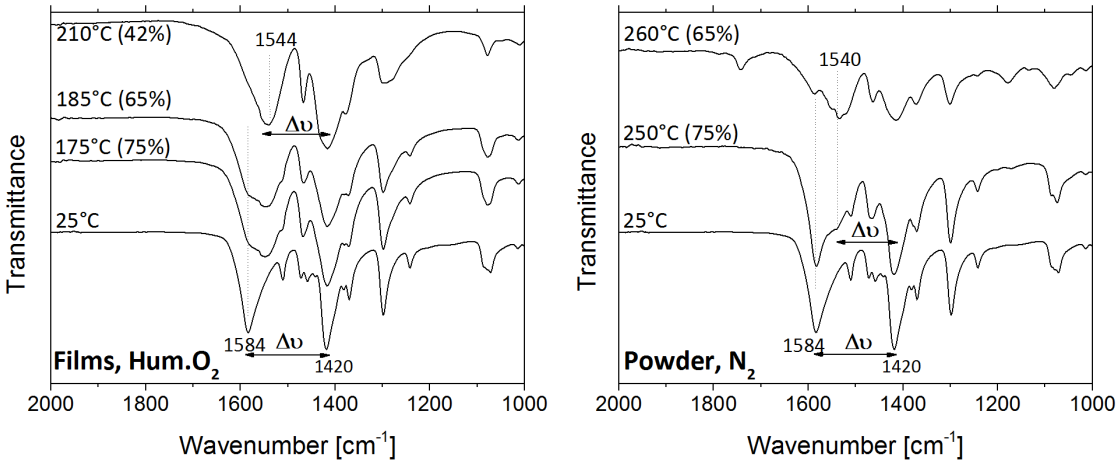

Fig. S5: *Enlargement of Fig.6 showing the evolution of the COO^- stretching band upon decomposition. Mass loss expressed as m/m_i is reported in brackets. $\Delta v=[v_{as}(COO^-)- v_s(COO^-)]$ goes from 165 to 125 cm^{-1} with increasing level of decomposition, suggesting a change in the structure. For films, the trend is similar in both humid O_2 and dry N_2.*

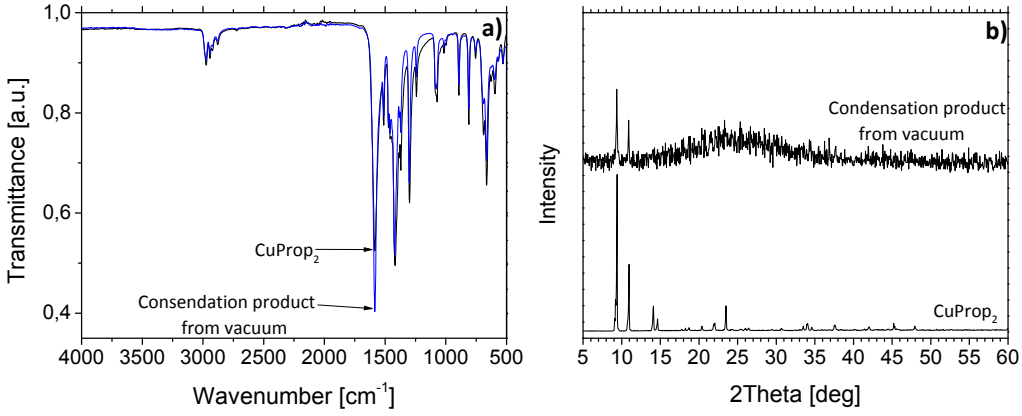

Fig. S6: *Comparison between $CuProp_2$ and the condensation product along the quartz tube coming from the decomposition in vacuum (E). a) FTIR spectrum and b) XRD patterns: the low signal to noise ratio for the upper spectrum is due to the very low amount of recovered product.*

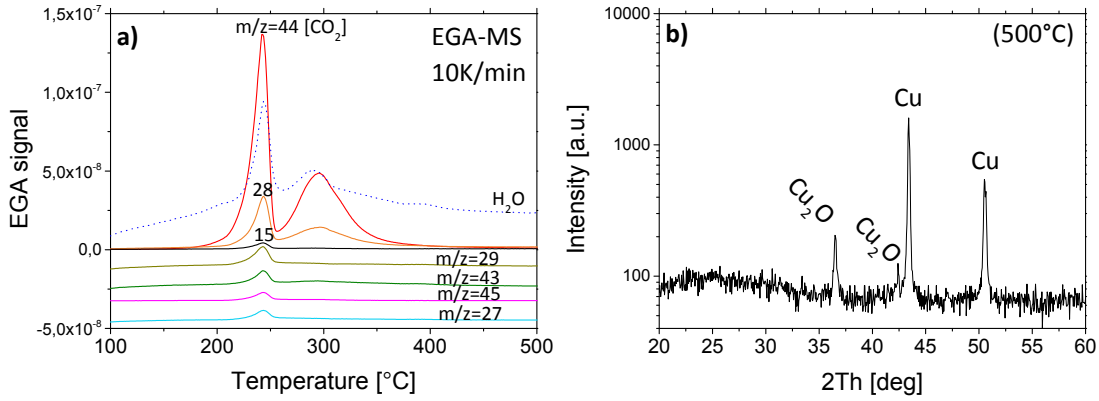

***Fig. S7**: (a): EGA-MS in vacuum of a quenched sample from experiment **A** (CuProp$_2$ film in humid O$_2$) at 210°C, before the II decomposition step takes place. (b): XRD pattern of the final decomposition product from (a) at 500°C*

The first peaks at 243°C show that the decomposition of the residual propionate produces acetaldehyde (m/z=29,43) and propionic acid (m/z=45) in very small amount, and, to a larger extent, water and CO/CO$_2$ (m/z=28,44 respectively). The last equilibrium may come from:

$$2CO \rightarrow C+CO_2$$

Oxidation of the organic ligand is accompanied by copper reduction. The first CO$_2$ peak in **Fig. S7** shows that simultaneously Cu(II) is reduced to Cu(I), and to Cu(0) later, with the second CO$_2$ peak:

$$4CuO + C \rightarrow 2Cu_2O + CO_2 \quad (243°C)$$
$$2Cu_2O + C \rightarrow 4Cu + CO_2 \quad (\sim 300°C)$$

The behavior is similar to when the entire decomposition of CuProp$_2$ in carried out in vacuum (Exp **E'-E''**); however, in this case (**Fig. S7**) Cu$_2$O is still present at 500°C, since not all CuO can be drastically reduced to Cu because the rest of the organic material necessary for this reduction has been decomposed in humid O$_2$.

Effect of sample layout and atmosphere on decomposition

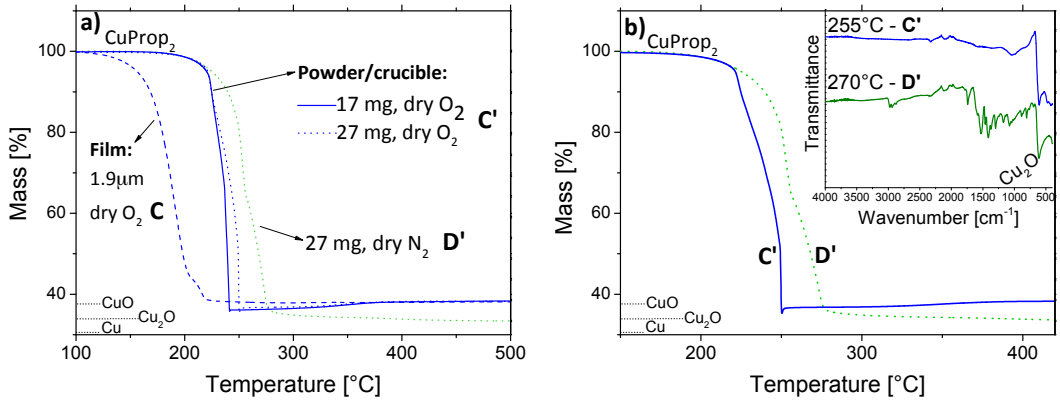

***Fig. S8**: Powders can create a locally inert atmosphere independently of the carrier gas: a) increasing the amount of powder decomposed in dry O$_2$, causes the curve to shift to higher temperatures, getting closer to the behavior of **D'**. The enlargement in b) shows that, simultaneously, the mass decreases as the curve shifts, until reaching values corresponding to the formation of Cu$_2$O/Cu (inset of b), as confirmed by the pink color of a quenched sample in O$_2$ at 255°C.*

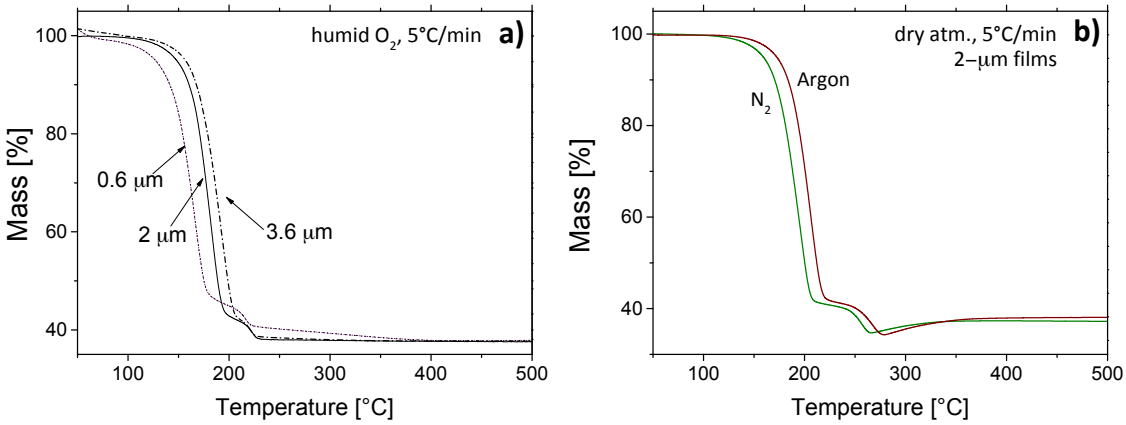

Fig. S9: *(a) Influence of film thickness on the decomposition of $CuProp_2$ in humid O_2. The thicker the film, the bigger the shift of the decomposition to higher temperatures. (b): influence of residual oxygen/water on the thermogravimetric curve of a film of $CuProp_2$: after 10-minute purge with 55-ml/min N_2 and after an hour purge in 80-ml/min Ar (with the addition of 60-ml/min Ar as reactive gas in the TGA). Since argon is heavier than nitrogen and was run for longer time and with higher flow, the residual humidity and O_2 content is expected to be lower, with subsequent shift of the curve to higher temperatures.*

Thermochemistry calculations with computational methods

The experimental values of enthalpy ($\Delta_r H$ exp) were obtained integrating the area of the differential scanning calorimetry (DSC) signal of the TG/DSC experiments with a straight base line in the temperature region corresponding to the decomposition peak. This area was then corrected by the mass (or moles) of the $CuProp_2$ involved in each mass-loss step, obtained from the information retained in the thermogravimetric curves. Thus, for all films except the case of dry N_2 (**D**), Stage II was normalized by the amount of remaining $CuProp_2$, undecomposed from Stage I. In the specific case of **D**, Stage II was normalized by the amount of CuO formed after Stage I and that undergoes reduction to Cu_2O.

Although the experimental values consisted of reaction enthalpies ($\Delta_r H$) at temperatures higher than room temperatures, the theoretical investigation was limited to the calculation of the electronic energy ($\Delta_r E$) of the corresponding reactions. Comparison of theoretical and experimental values is interesting due to the fact that it helps to rule out reaction schemes and to understand the main contribution of a given reaction to the decomposition path, but a more quantitative analysis was beyond the scope of this work.

Ab-initio theoretical calculations were performed within the framework of Density Functional Theory (DFT) as implemented in the VASP (Vienna Ab-initio Software Package) code. Database structure files for solids were obtained from the American Mineralogist Crystal Structure Database (AMCSD) for CuO (AMCSD code 0018812) and for $CuProp_2$ from the Cambridge Crystallographic Data Centre (CCDC code 1133510).

The electronic structure of the investigated molecules and materials was modelled using PAW (Projected Augmented Wave) potentials [S4] for the core electrons and plane-wave basis sets

with a 850 eV cutoff for valence. Electronic exchange and correlation effects were approximated using the Perdew-Burke-Ernzerhof (PBE) functional [S5]. Further corrections for long-range interactions were applied using the semi-empirical Grimme D3 dispersion model [S6]. Convergence of the electronic self-consistent field (SCF) calculations, set below a 10^{-5} eV threshold, was determined employing Blochl corrected smearing for calculation investigating solid materials, and Gaussian smearing for gas-phase molecules. Geometry optimizations were performed on all systems, using a 10^{-2} eV/Å force threshold. All such parameters were used as natively implemented in the code.

[S4] P. E. Blöchl, Phys. Rev. B 50 (1994) 17953–17979. doi:10.1103/physrevb.50.17953

[S5] J. P. Perdew, K. Burke and M. Ernzerhof, Phys. Rev. Lett. 77 (1996) 3865–3868. doi:10.1103/physrevlett.77.3865

[S6] S. Grimme, J. Antony, S. Ehrlich and H. Krieg, J. Chem. Phys. 132 (2010) 154104. doi: 10.1063/1.3382344

The following tables report raw data from our *ab-initio* calculations. Although vibrational frequency calculations for all the investigated systems have been considered, the computational time required to perform such calculation is very high and the quantitative accuracy that could be reached is out of the scope of this work, given the error associated with the experimental data.

	Stoichiometry of the unit cell	Total energy (eV)	Phase considered
$CuProp_2$	$C_{12}H_{20}O_8Cu_2$	-247.49663	solid
H_2O	H_2O	-14.246966	gas
CuO	Cu_4O_4	-40.836035	solid
Propionic acid	$C_3H_6O_2$	-63.414353	gas
CH_3CHO	C_2H_4O	-39.177523	gas
O_2	O_2	-9.899192	gas
CO_2	CO_2	-22.993639	gas
CO	CO	-14.80435	gas
Cu	Cu_4	-16.978334	solid

Table S2*: full energy values for the chemical species used for computational calculations.*

$CuProp_2$	
Cut-off energy (eV)	**Total single point energy (eV)**
300	-248.69583
350	-247.94709
400	-247.83637
450	-247.67543
500	-247.64114
550	-247.68015
600	-247.72871
650	-247.7701
700	-247.80947
750	-247.84161
800	-247.85653
850	-247.86855
900	-247.87161
950	-247.87224
1000	-247.87628

Table S3*: convergence of energy cut-off and K-mesh for* $CuProp_2$

Cu	
Cut-off energy (eV)	**Total single point energy (eV)**
350	-15.911244
375	-15.900787
400	-15.894942
425	-15.89210
450	-15.892295
475	-15.89230
500	-15.892874

Table S4*: convergence of energy cut-off and K-mesh for Cu*

CuO	
Cut-off energy (eV)	**Total single point energy (eV)**
300	-41.4808
400	-40.8889
500	-40.8168
600	-40.8229
700	-40.8322
800	-40.836
900	-40.8357
1000	-40.8354

Table S5*: convergence of energy cut-off and K-mesh for CuO*

Convergence for the k-point mesh was performed only on solid phase supercells, as gas phase cells are optimized to minimize the interaction between replicas, and are therefore requiring a single K-point to describe their non-periodic electronic structure.

Computational models

CuProp$_2$:

(C12 H20 Cu2 O8)n
1.00000000000000
5.2341858657588070 0.0339663069233462 -0.0200572110250093
-2.1585027167178890 8.0161529042647768 0.0254562892695177
-0.3382044427006869 -0.3537485092471030 9.5589594192681950
Cu2 O8 C12 H20
Direct
0.2217592134421721 0.0234568785834117 0.0646043311144497
0.7782407835578242 0.9765431304165926 0.9353956978855491
0.3370778348454527 0.9433452362903707 0.8800483771329358
0.6629221741545378 0.0566547007096348 0.1199516078670666
0.0641149288281170 0.0992683953663205 0.2324648077122886
0.9358849941718802 0.9007315316336838 0.7675352652877139
0.1051431077711935 0.7922462069735026 0.1294055623503715
0.8948568912288027 0.2077537600264910 0.8705944216496271
0.2908044591009773 0.2496640823775786 0.9906366196857350
0.7091955588990169 0.7503359176224214 0.0093634503142634
0.1813042799218282 0.9070448257430397 0.7703560577505133
0.8186956220781705 0.0929551272569597 0.2296439392494824
0.3024748167548005 0.8777517596897872 0.6340851448248415
0.6975251842451957 0.1222482023102101 0.3659149021751590
0.1092952599795061 0.7750449840289582 0.5225318476344351
0.8907047670204921 0.2249549849710432 0.4774682003655611
0.8718474851179119 0.7054455890488069 0.0935460629768076
0.1281524728820911 0.2945543959511944 0.9064539910231900
0.7723508677296931 0.5376109298293473 0.1582995353998747
0.2276492152703026 0.4623890391706458 0.8417004996001251
0.5487928101280400 0.5420763905022519 0.2564801800531011
0.4512072648719628 0.4579235804977495 0.7435198919468985
0.3891863277903800 0.0042425488784360 0.5976064470175497
0.6108136722096209 0.9957574381215594 0.4023936499824475
0.4717345040464442 0.8255610894054560 0.6574771471293270
0.5282655129535607 0.1744388815945450 0.3425229248706712
0.2065811435374959 0.7684546889341525 0.4237117261740464
0.7934189524625049 0.2315453100658438 0.5762883208259533
0.0278297533790159 0.6472077798695113 0.5560373338421957
0.9721702626209855 0.3527922181304890 0.4439627141578080
0.9432163047817973 0.8306310519386827 0.5013798444410925
0.0567837232182054 0.1693689470613208 0.4986202025589079
0.6950096881045489 0.4438879427108839 0.0736462899246964

0.3049903478954540 0.5561120572891088 0.9263537890753062
0.9383566866380973 0.5045399129337852 0.2139242482609007
0.0616433953619030 0.4954600270662176 0.7860757867390994
0.4522556447055234 0.4159010191564443 0.2884676490005824
0.5477443462944722 0.5840989218435545 0.7115323979994180
0.6239874391634612 0.6200766844453752 0.3510535293873029
0.3760126008365420 0.3799233435546208 0.6489465176126973
0.3987711197748003 0.5931858376832307 0.2031285666219347
0.6012288722251987 0.4068141323167664 0.7968714803780726

H_2O:

POSCAR_H2O
1.00000000000000
20.0000000000000000 0.0000000000000000 0.0000000000000000
0.0000000000000000 20.0000000000000000 0.0000000000000000
0.0000000000000000 0.0000000000000000 20.0000000000000000
O1 H2
Direct
0.1799999999999997 0.2500000000000000 0.3268327649895385
0.1799999999999997 0.2884483614597593 0.3565836175052268
0.1799999999999997 0.2115516385402406 0.3565836175052268

CuO:

cu1 o1
1.00000000000000
4.4349489164138074 0.0000000000000000 0.0000663801113373
0.0000000000000000 3.6247446279274373 0.0000000000000000
-0.8038614658969085 0.0000000000000000 5.0697704857559414
Cu4 O4
Direct
0.2446619397060800 0.2504016073117590 0.0049787504010736
0.2446619377060798 0.7495984096882390 0.5049787524010738
0.7446619647060786 0.7504015903117610 0.0049787504010736
0.7446619627060784 0.2495984096882387 0.5049787524010738
0.9949380222939197 0.4407991667280202 0.2552212545989279
0.9949380202939195 0.5592008332719798 0.7552212565989280
0.4949380732939205 0.9407991667280202 0.2552212545989279
0.4949380712939204 0.0592008422719770 0.7552212565989280

Propionic acid:

1.00000000000000
20.0000000000000000 0.0000000000000000 0.0000000000000000
0.0000000000000000 20.0000000000000000 0.0000000000000000
0.0000000000000000 0.0000000000000000 20.0000000000000000
C3 H6 O2
Direct

0.2528501645437676 0.1718332274177514 0.1647444699569063
0.1888712120261260 0.1304351572870674 0.1647444273861480
0.1261851080510029 0.1725176960234160 0.1648172152190912
0.2968981712259368 0.1390400188041295 0.1647177573274195
0.2553989481825656 0.2042857779961977 0.1205380708464887
0.2554149757723596 0.2042390865279778 0.2089829578644509
0.1861673175697838 0.0970371058875129 0.1209825762281338
0.1862192269375199 0.0969704491049794 0.2084551954643423
0.0318575846207900 0.1643607920117251 0.1648537148086930
0.1236232457546340 0.2334352561392738 0.1647748561336364
0.0699046841654985 0.1334611992999735 0.1649446083146915

CH_3CHO:

1.00000000000000
20.0000000000000000 0.0000000000000000 0.0000000000000000
0.0000000000000000 20.0000000000000000 0.0000000000000000
0.0000000000000000 0.0000000000000000 20.0000000000000000
C2 H4 O1
0.1383470993495132 0.0774406349970845 0.0919250011500026
0.0685318920662174 0.1050978270741086 0.0919250011500026
0.1655542720120260 0.0963829655799082 0.1359616899636280
0.1655542720120260 0.0963829655799082 0.0478883063363695
0.0650528363323001 0.1610828517764148 0.0919250011500026
0.1380886631544539 0.0226337636335462 0.0919250011500026
0.0177208437234604 0.0713816994590298 0.0919250011500026

O_2:

POSCAR_O2
1.0
+20.0000000000 +0.0000000000 +0.0000000000
+0.0000000000 +20.0000000000 +0.0000000000
+0.0000000000 +0.0000000000 +20.0000000000
O2
Cartesian
+3.6000000000 +4.8833525920 +6.6000000000
+3.6000000000 +6.1166474080 +6.6000000000

CO_2:

POSCAR_CO2
1.0
+20.0000000000 +0.0000000000 +0.0000000000
+0.0000000000 +20.0000000000 +0.0000000000
+0.0000000000 +0.0000000000 +20.0000000000
C1 O2
Cartesian
+3.6000000000 +5.0000000000 +6.6000000000
+3.6000000000 +6.1767554630 +6.6000000000

+3.6000000000 +3.8232445370 +6.6000000000

CO:

POSCAR_CO
1.0
+20.0000000000 +0.0000000000 +0.0000000000
+0.0000000000 +20.0000000000 +0.0000000000
+0.0000000000 +0.0000000000 +20.0000000000
C1 O1
Cartesian
+3.6000000000 +5.1784203896 +6.6000000000
+3.6000000000 +6.3215796104 +6.6000000000

Cu:

mn1
1.00000000000000
3.8619999886000000 0.0000000000000000 0.0000000000000000
0.0000000000000000 3.8619999886000000 0.0000000000000000
0.0000000000000000 0.0000000000000000 3.8619999886000000
Cu4
Direct
0.0000000000000000 0.0000000000000000 0.0000000000000000
0.0000000000000000 0.5000000000000000 0.5000000000000000
0.5000000000000000 0.0000000000000000 0.5000000000000000
0.5000000000000000 0.5000000000000000 0.0000000000000000